Nanoscale

ROYAL SOCIETY OF CHEMISTRY

PAPER

View Article Online
View Journal | View Issue

Cite this: *Nanoscale*, 2024, **16**, 10273

NIR-II light powered hydrogel nanomotor for intravesical instillation with enhanced bladder cancer therapy†

Wei Chen,‡[a] Yingfei Wang,‡[b,d] Hao Hu,[a] Yu Zhu,[b] Hongxia Zhao,[b] Jie Wu,[b] Huangxian Ju,[b] Qing Zhang,*[a] Hongqian Guo*[a] and Ying Liu*[b,c]

Intravesical instillation is the common therapeutic strategy for bladder cancer. Besides chemo drugs, nanoparticles are used as intravesical instillation reagents, offering appealing therapeutic approaches for bladder cancer treatment. Metal oxide nanoparticle based chemodynamic therapy (CDT) converts tumor intracellular hydrogen peroxide to ROS with cancer cell-specific toxicity, which makes it a promising approach for the intravesical instillation of bladder cancer. However, the limited penetration of nanoparticle based therapeutic agents into the mucosa layer of the bladder wall poses a great challenge for the clinical application of CDT in intravesical instillation. Herein, we developed a 1064 nm NIR-II light driven hydrogel nanomotor for the CDT for bladder cancer *via* intravesical instillation. The hydrogel nanomotor was synthesized *via* microfluidics, wrapped with a lipid bilayer, and encapsulates CuO_2 nanoparticles as a CDT reagent and core–shell structured Fe_3O_4@Cu_9S_8 nanoparticles as a fuel reagent with asymmetric distribution in the nanomotor (LipGel-NM). An NIR-II light irradiation of 1064 nm drives the active motion of LipGel-NMs, thus facilitating their distribution in the bladder and deep penetration into the mucosa layer of the bladder wall. After FA-mediated endocytosis in bladder cancer cells, CuO_2 is released from LipGel-NMs due to the acidic intracellular environment for CDT. The NIR-II light powered active motion of LipGel-NMs effectively enhances CDT, providing a promising strategy for bladder cancer therapy.

Received 15th March 2024,
Accepted 24th April 2024

DOI: 10.1039/d4nr01128g

rsc.li/nanoscale

Introduction

Bladder cancer is among the most common cancers worldwide[1–4] and severely threatens human health with a 50% risk of recurrence and a 20% risk of progression within five years.[5] Intravesical instillation, which exposes tumor sites to high local concentrations of therapeutic drugs, is the classical clinical therapy for bladder cancer and is used as an adjuvant treatment after transurethral resection of the bladder tumor to reduce the recurrence rate and prevent progression.[6]

Nanoparticles, and corresponding therapies relied on nanoparticles such as chemodynamic therapy (CDT) that converts tumor intracellular hydrogen peroxide to ROS with cancer cell-specific toxicity,[7–11] have been coupled with intravesical instillation and have introduced new therapy strategies for bladder cancer treatment.[12–19] The penetration capability of the poured reagent is important for the therapeutic efficiency of intravesical instillation. However, unlike small molecule drugs, the size of nanoparticles impairs their diffusion and penetration in the tumor tissue.[20] Therefore, powering nanoparticle reagents with continuous driving force in intravesical instillation would improve their active transportation in the tumor position.

Nanoparticles that are equipped with driving motors convert diverse energy sources into autonomous mechanical motion, which improves their tumor penetration and biodistribution.[21–24] Urease functionalized nanomotors that catalyze the conversion of urea into carbon dioxide and ammonia as motion driving force have been reported as intravesical instillation reagents, which deeply penetrate into the mucosa layer of the bladder wall and thus provide efficient delivery of treatment drugs for various bladder diseases.[25] However, the random distribution of urease on the nanomotor's surface and inevitably decreased enzyme activity by the bladder's harsh microenvironment impairs the motion efficacy of urease-equipped nanomotors as intravesical instillation reagents.

As an external stimulus with high penetration and low photo scattering, NIR light irradiation provides a stable and

[a]*Nanjing Drum Tower Hospital Clinical College of Nanjing University of Chinese Medicine, Nanjing 210008, PR China*
[b]*State Key Laboratory of Analytical Chemistry for Life Science, School of Chemistry and Chemical Engineering, Nanjing University, Nanjing 210023, PR China*
[c]*Chemistry and Biomedicine Innovation Center, Nanjing University, Nanjing 210023, PR China. E-mail: yingliu@nju.edu.cn*
[d]*State Key Laboratory of Digital Medical Engineering, School of Biological Science and Medical Engineering, Southeast University, Nanjing 210096, PR China*
†Electronic supplementary information (ESI) available. See DOI: https://doi.org/10.1039/d4nr01128g
‡Equal contribution.

powerful driving force for nanomotor motion.[26–28] Most reported nanomotors rely on noble metals such as Au and Pt with a driving force of NIR light up to 1000 nm to propel nanomotors.[29–36] Considering the irradiation light with longer wavelength provides deeper penetration, lower tissue autofluorescence and photo scattering,[37–39] herein, we develop a 1064 nm NIR-II light-driven nanomotor for CDT of bladder cancer *via* intravesical instillation. The NIR-II light-driven nanomotor is a lipid bilayer encapsulated hydrogel nanoparticle with asymmetric encapsulation of chemodynamic therapeutic reagent CuO_2 nanoparticles and fuel reagent core–shell structured Fe_3O_4@Cu_9S_8 nanoparticles (LipGel-NM), which has powerful motion efficacy with enhanced penetration depth on bladder wall and CDT effect. To synthesize LipGel-NMs, lipid bilayer encapsulated hydrogel nanodroplets (LipGel-NDs) containing CuO_2 NPs and Fe_3O_4@Cu_9S_8 NPs are synthesized *via* a flow-focusing based microfluidic mixing approach that we previously reported.[40] The as-obtained LipGel-NDs are then left standing on top of a magnet overnight, which concentrates Fe_3O_4@Cu_9S_8 NPs into the clusters and precipitates them to the bottom of LipGel-NDs. 50 s of UV light exposure is then performed to convert nanodroplets to nanoparticles LipGel-NMs with the asymmetric distribution of Fe_3O_4@Cu_9S_8 NPs at one portion. Localized surface plasmon resonance (LSPR) of Cu_9S_8 in the NIR-II region endows them with intensive photothermal properties, and their asymmetric distribution results in temperature gradients inside LipGel-NMs for thermophoresis propulsion of nanomotors. A folic acid (FA) decorated lipid bilayer coating facilitates cancer cell targeting and prevents leakage of CuO_2 before cancer cell endocytosis. After intravesical instillation of LipGel-NMs, non-invasive 1064 nm NIR-II light irradiation is performed at the bladder area, which drives the active motion of nanomotors to facilitate their distribution in the bladder and deep penetration into the mucosa layer of the bladder wall (Scheme 1, deep tissue penetration). After FA-mediated endocytosis in bladder cancer cells, the lipid bilayer of LipGel-NMs is decomposed by the acidic intracellular environment to release CuO_2 for CDT (Scheme 1, enhanced chemodynamic therapy). The NIR-II light powered active motion of LipGel-NMs effectively enhances the CDT for bladder cancer.

Results and discussion

Preparation and characterization of LipGel-NMs

CuO_2 NPs were prepared according to a previously reported method[41,42] by reacting $CuCl_2{\cdot}2H_2O$ and H_2O_2 in the NaOH solution containing PVP at room temperature for 20 min (Fig. S1†). TEM images demonstrated that the as-prepared CuO_2 NPs were 6.47 ± 1.17 nm in diameter (Fig. 1A and Fig. S2A†). CuO_2 was well-dispersed in water with a mean hydrodynamic diameter of ~17.9 nm (Fig. S2B†) and zeta potential of 13.9 ± 0.833 mV. Powder X-ray diffraction (XRD) pattern and XPS spectrum of the as-obtained CuO_2 NPs were consistent with literature-reported characteristic peaks of CuO_2 NPs,[41] indicating the successful synthesis of CuO_2 NPs (Fig. S2C and D†). CuO_2 NPs were converted into Cu^{2+} and H_2O_2 in an acidic solution, which induced cuproptosis with self-supplied H_2O_2.[41–43] To confirm its H_2O_2 generation capability, CuO_2 NPs were dispersed in an acidic solution and reacted with MnO_4^-. The as-produced H_2O_2 efficiently reduced MnO_4^- to Mn^{2+}, and suppressed its characteristic absorption peak in the 450–600 nm region (Fig. 1B, CuO_2). H_2O_2 also caused absorption suppression for MnO_4^-, while incubating with Cu^{2+} barely decreased MnO_4^- absorbance (Fig. 1B, H_2O_2, Cu^{2+}). Cu^{2+} reacted with H_2O_2 *via* a Fenton-like reaction,[44,45] and the as generated $^{\cdot}OH$ was confirmed using the methylene blue (MB) assay. Co-incubating MB with Cu^{2+} and H_2O_2 resulted in a rapid decrease of MB characteristic absorption at 664 nm (Fig. S2E,† Cu^{2+} + H_2O_2). To verify the capability of CuO_2 NPs for Fenton-like reaction and corresponding $^{\cdot}OH$

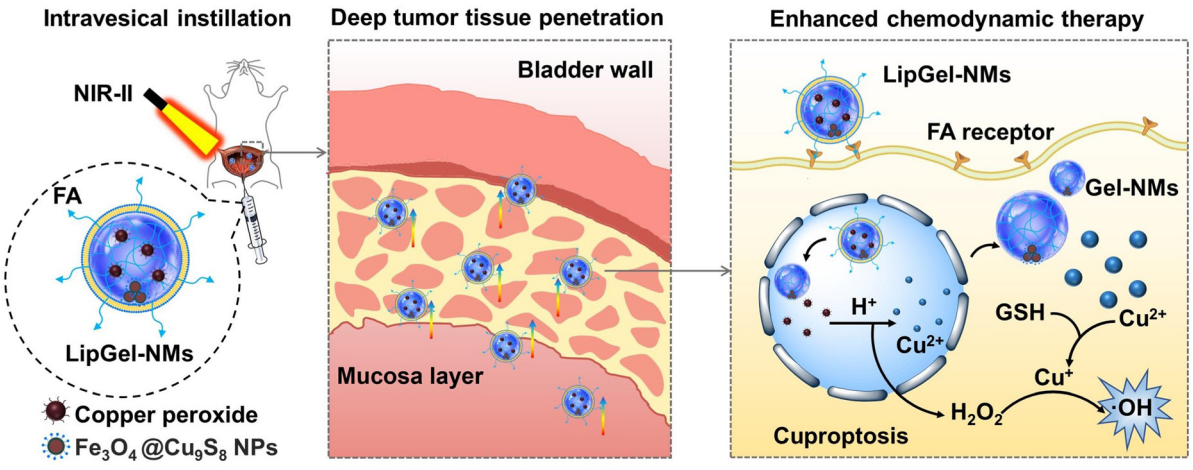

Scheme 1 Schematic illustration for the intravesical instillation of the lipid bilayer coated hydrogel nanomotors with the encapsulation of CuO_2 NPs (LipGel-NMs) for enhanced chemodynamic therapy of bladder cancer.

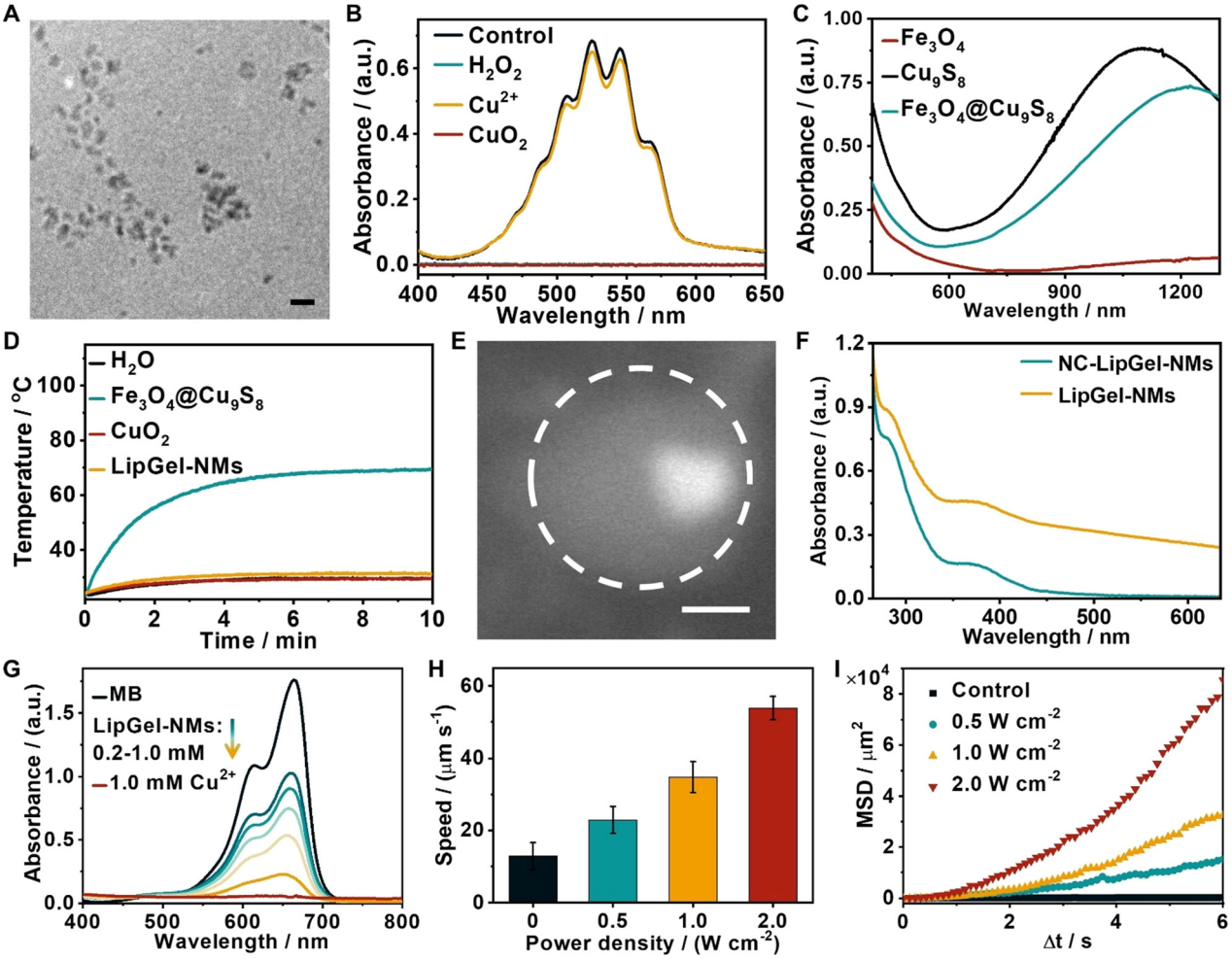

Fig. 1 (A) TEM image of CuO_2 NPs (scale bar: 50 nm). (B) UV-vis absorption spectra of MnO_4^- (control) and MnO_4^- incubated with H_2O_2 (H_2O_2), Cu^{2+} (Cu^{2+}), and CuO_2 (CuO_2). (C) UV–vis absorption spectra of the chloroform dispersed Fe_3O_4 core and water dispersed $Fe_3O_4@Cu_9S_8$ NPs. Cu_9S_8 NPs were set as control. (D) Time-dependent temperature increase in H_2O, $Fe_3O_4@Cu_9S_8$ NPs, CuO_2 and LipGel-NMs in response to NIR-II irradiation (1 W cm^{-2}). (E) SEM image of LipGel-NMs; scale bar: 100 nm. (F) UV-vis absorption spectra of NC-LipGel-NMs and LipGel-NMs. (G) UV-vis absorption spectra of MB aqueous solution and MB aqueous solution corresponding to LipGel-NMs with equivalent CuO_2 concentrations of 0.2, 0.4, 0.6, 0.8, and 1.0 mM, and 1.0 mM. (H) Motion speeds of LipGel-NMs under different NIR-II power densities from 0–2.0 W cm^{-2}, and (I) their corresponding MSD plots (6 s). Error bars indicate mean ± SD (n = 10).

generation, CuO_2 NP-dispersed acidic solution (pH 6.0) was incubated with MB, which led to an efficient decrease for MB characteristic absorption peak (Fig. S2E,† pH 6.0). On the contrary, the incubating neutral solution (pH 7.4) dispersed CuO_2 NPs with MB barely decreased its characteristic absorption peak (Fig. S2E,† pH 7.4). These results confirmed CuO_2 NPs as an ideal CDT reagent for $^{\bullet}$·OH generation.

Core–shell structured $Fe_3O_4@Cu_9S_8$ NPs were prepared according to our previously reported method (Fig. S3A†).[40,46,47] Spherical-shaped Fe_3O_4 core was synthesized first with Fe(acac)$_3$ precursor in oleylamine with diameter of 6.91 ± 0.99 nm, which contributed to the magnetic property of $Fe_3O_4@Cu_9S_8$ NPs (Fig. S3B and S3C,† Fe_3O_4). Continuous reaction with the Cu(acac)$_2$ precursor resulted in the coating of the Cu_9S_8 shell on the Fe_3O_4 core. The as-obtained core–shell structured $Fe_3O_4@Cu_9S_8$ with oleylamine as the stabilizing ligand ($Fe_3O_4@Cu_9S_8$-OA NPs) demonstrated a diameter of 8.47 ± 1.08 nm (Fig. S3B and S3C,† $Fe_3O_4@Cu_9S_8$-OA). The powder X-ray diffraction (XRD) pattern of $Fe_3O_4@Cu_9S_8$-OA was indexed as a mixture of the face-centered cubic Fe_3O_4 (PDF#19-0629) and hexagonal Cu_9S_8 (PDF#36-0379) phases (Fig. S4A†). XPS spectra demonstrated characteristic peaks for S splitting 2p, Cu 2p3, and Cu 2p1 at 166.0, 932.7, and 952.7 eV, respectively, for $Fe_3O_4@Cu_9S_8$-OA (Fig. S4B†), which was consistent with literature reported characteristic peaks for Cu_9S_8,[40,47] indicating the successful coating of Cu_9S_8 on the Fe_3O_4 core. To disperse $Fe_3O_4@Cu_9S_8$-OA in aqueous solution and facilitate subsequent polymerization with hydrogel precursor, DSPE-PEG-acrylate, as an amphiphilic ligand, was coated on $Fe_3O_4@Cu_9S_8$-OA *via* hydrophobic–hydrophobic interaction of DSPE and OA to prepare water-soluble $Fe_3O_4@Cu_9S_8$ NPs.[48–50] The as-obtained $Fe_3O_4@Cu_9S_8$ NPs demonstrated much-improved dispersity in

water (Fig. S5A†) and a similar diameter of 9.85 ± 2.28 nm (Fig. S5B and C†) with a zeta potential of −3.76 ± 0.627 mV. The as-obtained Fe_3O_4@Cu_9S_8 NPs demonstrated an intense absorption band at *ca.* 1100 nm due to the localized surface plasmon resonances (SPR) in the vacancy-doped outer shell Cu_9S_8 (Fig. 1C). The strong adsorption endowed Fe_3O_4@Cu_9S_8 NPs with good NIR-II photothermal capability, which corresponds with previous reports.[51,52] Fe_3O_4@Cu_9S_8 NPs demonstrated rapid temperature increase and reached 66.5 °C within 5 min upon 1064 nm light irradiation (Fig. 1D).

A two-inlets flow-focusing configured microfluidic chip that was set up with a FLOW-EZ pump and a microscope (Fig. S6A†) was used to prepare LipGel nanodroplets (LipGel-NDs), which contained Fe_3O_4@Cu_9S_8 NPs and CuO_2 NPs with FA labelled bilayer lipid membrane as a coating layer. The lipid precursor containing IPA-dispersed lecithin, cholesterol, DSPE-PEG and DSPE-PEG-FA was brought into the central channel. The hydrogel precursor containing water-dispersed PEG-DA-575, Fe_3O_4@Cu_9S_8 NPs, CuO_2 NPs and photoinitiator 2-hydroxy-2-methyl-propiophenone was brought into the side channels (Fig. S6B†). The side channel hydrogel precursor flow was kept at a higher rate than the central lipid precursor flow, which squeezed the central lipid precursor flow into a narrow stream at the intersection point for focusing of the hydrodynamic flow. The IPA phase and aqueous phase were mixed *via* diffusion at the laminar interface to the point where the concentration of lipids exceeded its critical micelle concentration, therefore, forming liposomes as LipGel-NDs (Fig. S7A†).

To prepare LipGel-NMs with asymmetric distribution of Fe_3O_4@Cu_9S_8 NPs, the above-obtained LipGel-NDs were put under a magnetic field to concentrate Fe_3O_4@Cu_9S_8 NPs to a point at the edge of LipGel-NDs. Subsequent photo-polymerization with PEG-DA fixed the asymmetric distribution of Fe_3O_4@Cu_9S_8 and converted LipGel-NDs to LipGel-NMs (Fig. S7B†). The FTIR spectrum of PEG-DA showed characteristic peaks for –C═O and –C═C– stretching vibrations at 1721 cm^{-1} and 1636 cm^{-1}, respectively (Fig. S8,† PEG-DA precursor). After UV irradiation, the successful polymerization of PEG-DA was confirmed by the reduction of the –C═C– characteristic peak in the FTIR spectrum (Fig. S8,† hydrogel). SEM characterization showed LipGel-NMs of around 350 nm with Fe_3O_4@Cu_9S_8 NPs of around 110 nm located at one edge of LipGel-NMs (Fig. 1E). Fe_3O_4@Cu_9S_8 NPs occupied ∼2.1% of LipGel-NMs volume. LipGel-NMs demonstrated a hydrodynamic diameter of 403 ± 11.1 nm (Fig. S9†) and zeta potential of −7.03 ± 0.202 mV due to the existence of FA on the bilayer lipid membrane coating layer. The content of CuO_2 NPs was determined to be 83.4 μg mg^{-1} of LipGel-NMs, which enhanced UV-vis absorption in the region above 300 nm for LipGel-NMs compared with noncurative LipGel-NMs that were not encapsulated CuO_2 NPs (NC-LipGel-NMs) (Fig. 1F). The encapsulated CuO_2 NPs decomposed to Cu^{2+} in the acid environment, along with the degradation of the liposome wrapping layer to release Cu^{2+}.[41,42,53] Cu^{2+} release efficiency was evaluated by ICP-MS, which was saturated at 58.31% in 24 h at pH 6.0 (Fig. S10,† pH 6.0). Cu^{2+} release was largely suppressed at pH 7.4 (Fig. S10,† pH 7.4), indicating the satisfactory suppression of Cu^{2+} leakage during the delivery process. To verify the capability of LipGel-NMs for $^{\bullet}OH$ generation, MB was incubated with various concentrations of LipGel-NMs (denoted as equivalent CuO_2 concentration) at pH 6.0, which demonstrated a gradual intensity decrease of the MB characteristic absorption peak according to the concentration (Fig. 1G) of LipGel-NMs.

The asymmetric distribution of the Fe_3O_4@Cu_9S_8 cluster at one edge of LipGel-NMs made it a heat source under NIR-II irradiation and generated a temperature gradient inside LipGel-NMs. The corresponding self-thermophoresis resulted in the powerful motion of LipGel-NMs. The motion videos (Movies S1–S4†) and time-lapse images (Fig. S11†) of LipGel-NMs under different 1064 nm NIR-II irradiation power densities showed an increased motion speed with enhanced power densities from 0.5 to 2.0 W cm^{-2} (Fig. 1H). Though it caused a temperature gradient inside LipGel-NMs, the 1064 nm NIR-II irradiation to LipGel-NMs did not affect the environment temperature due to the small portion of Fe_3O_4@Cu_9S_8 cluster in LipGel-NMs and poor thermal conductivity of PEG hydrogel (0.24 W m^{-1} K^{-1}). LipGel-NMs dispersed solution showed a similar extent of temperature change as water in response to 1064 nm NIR-II irradiation (Fig. 1D, LipGel-NMs). The motion of LipGel-NMs in cell culture media supplemented with 10% FBS demonstrated a similar tendency towards increased NIR-II laser power densities with slightly lower motion speeds (Movies S5–S8 and Fig. S12A, B†). Mean square displacement (MSD) for LipGel-NMs under different 1064 nm NIR-II laser irradiation power densities in PBS (Fig. 1I) and cell culture media (Fig. S12C†) demonstrated quadratic functions of time, confirmed that LipGel-NMs' movement originated from thermophoresis effect rather than a heat enhanced Brown motion. The *in vitro* swarming behavior of LipGel-NMs was investigated in a horizontally positioned glass capillary (inner diameter of 500 μm) filled with water to further confirm the LipGel-NMs motion under 1064 nm NIR-II irradiation. Cy7.5-labeled LipGel-NMs (LipGel-NMs-Cy7.5) were prepared with a PEG-DA-Cy7.5 dispersed hydrogel precursor and seeded at the edge of each capillary. Fluorescence photos were acquired by a home-built NIR-II microscope after 25 min of incubation in the presence and absence of 10 min NIR-II light irradiation. LipGel-NMs with 10 min NIR-II irradiation diffused to further place in glass capillary (Fig. S13A and B,† NIR-II(+)) compared with non-irradiated ones (Fig. S13A and B,† NIR-II(−)), indicating the active motion of LipGel-NMs with NIR-II irradiation.

Characterization of the therapeutic effect of LipGel-NMs at the cellular level

NIR-II irradiation propelled LipGel-NMs facilitated their active transportation from exterior tumor tissue to the interior as well as the endocytosis process.[33,35,36] To monitor the endocytosis process of nanomotors, Cy3 labelled LipGel-NMs (LipGel-NMs-Cy3) was prepared with PEG-DA-Cy3 dispersed hydrogel precursor, and incubated with MB49 cells. NIR-II irradiation facilitated the fast accumulation of LipGel-NMs-Cy3 around

MB49 cells and showed intense intracellular Cy3 fluorescence that well co-localized with Lyso-Tracker fluorescence (Fig. 2A, NIR-II(+)). The control group MB49 cells were incubated with LipGel-NMs-Cy3 in the absence of NIR-II light irradiation and demonstrated negligible intracellular Cy3 fluorescence (Fig. 2A, NIR-II(−)). A long incubation time of 180 min was required to observe LipGelNMs-CP-Cy3 fluorescence from MB49 cells without NIR-II irradiation (Fig. S14A†). These results indicated the contribution of NIR-II light irradiation to the endocytosis process. To evaluate the delivery specificity of LipGel-NMs, NF-LipGel-NMs-Cy3 were incubated with MB49 cells for 25 min in the presence of NIR-II light irradiation, which demonstrated negligible intracellular Cy3 fluorescence (Fig. S14B†). To trace the endocytosis pathway of LipGel-NMs, MB49 cells were incubated with LipGel-NMs-Cy3, which showed an obvious overlap of Cy3 fluorescence and Lyso-Tracker fluorescence in 60 min incubation with a clear separation of two fluorescence in 180 min incubation, indicating successful endosome escape of LipGel-NMs (Fig. S15†).

The capability of LipGel-NMs permeating into the tumor environment was evaluated by transwell experiments. To mimic the process of nanomotors translating from the blood vessel to the tumor site, two-dimensional cellular models were established by seeding HUVEC cells in the upper chamber and MB49 cells in the lower chamber (Fig. 2B).[54–56] The upper HUVECs were treated with LipGel-NMs-Cy3 in the presence and absence of NIR-II irradiation respectively, and subsequently co-incubated with the lower chamber. Cy3 fluorescence was negligible from MB49 cells that were seeded in the lower chamber for the group in the absence of NIR-II laser irradiation (Fig. 2C, NIR-II(−)), while bright Cy3 fluorescence was observed from MB49 cells for the group with NIR-II irradiation (Fig. 2C, NIR-II(+)). This result indicated the contribution of NIR-II light as a driving force to the permeation behavior of LipGel-NMs from the blood vessel to the tumor site. A similar transwell experiment was performed with MB49 cells seeded both in the upper and lower chambers to verify the intratumoral penetration capability of LipGel-NMs

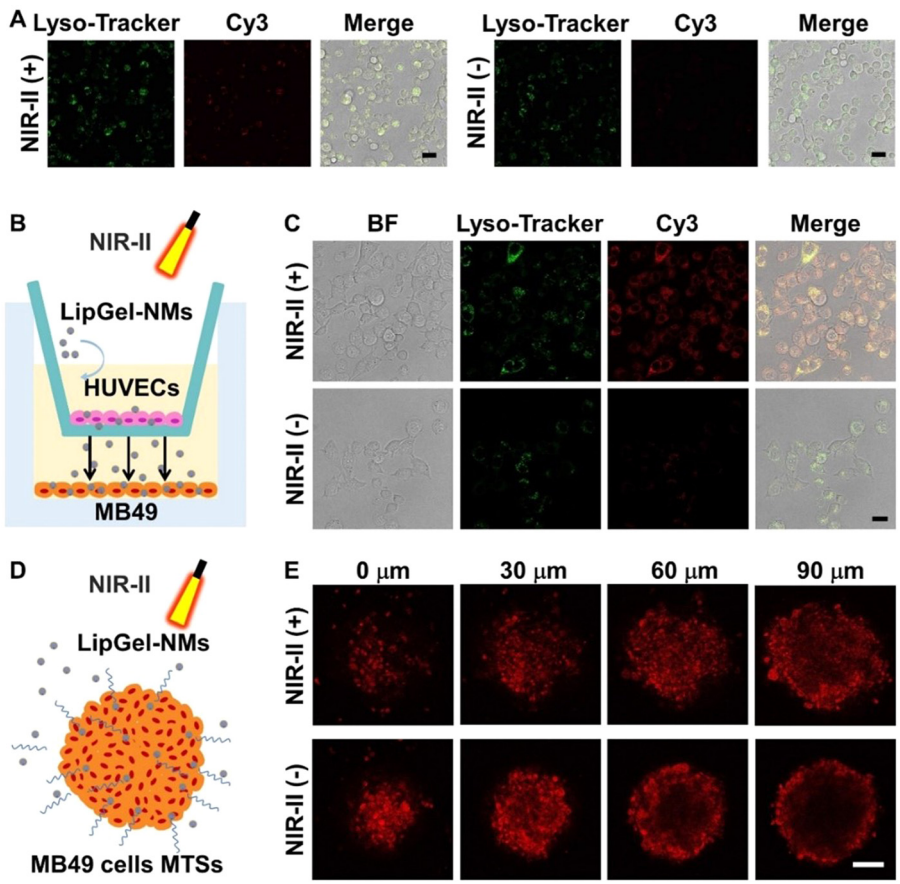

Fig. 2 (A) CLSM images of MB49 cells incubated with LipGel-NMs-Cy3 in the presence (NIR-II(+)) and absence (NIR-II(−)) of 10 min NIR-II irradiation (scale bar: 20 μm). (B) Schematic illustration of the transvascular extravasation model with HUVEC cells in the upper chamber and MB49 cells in the bottom chamber, and (C) CLSM images of MB49 cells in the bottom chamber in the presence (NIR-II(+)) and absence (NIR-II(−)) of NIR-II irradiation (scale bar: 20 μm). (D) Schematic illustration of MB49 cell 3D MTS model incubated with LipGel-NMs-Cy3 and (E) *Z*-stack CLSM images of 3D MTSs planes with different distances to the bottom of 3D MTSs in the presence (NIR-II(+)) and absence (NIR-II(−)) of NIR-II irradiation (scale bar: 100 μm). Red channel (Cy3) fluorescence was collected at 555–605 nm with 543 nm excitation, and green channel (Lyso-Tracker Green) fluorescence was collected at 505–555 nm with 488 nm excitation.

(Fig. S16A†). CLSM images demonstrated similar results with much stronger Cy3 fluorescence from MB49 cells that were seeded in the lower chamber with NIR-II light irradiation compared with the group in the absence of NIR-II light irradiation (Fig. S16B†), indicating NIR-II light irradiation facilitated intratumoral penetration of LipGel-NMs as well.

A three-dimensional (3D) multicellular tumor spheroids (MTSs) model was set up to simulate the spatial complexity and heterogeneity of tumor tissues (Fig. 2D). CLSM *z*-stack imaging was conducted at different sections of 3D MB49 MTSs from the bottom to evaluate the diffusion of LipGel-NMs-Cy3 in MTSs (Fig. 2E). NIR-II light irradiation effectively enhanced the penetration depth of LipGel-NMs-Cy3 in 3D MTSs, and Cy3 fluorescence was almost observed in the whole section area 90 μm away from the bottom (Fig. 2E, NIR-II(+)). On the contrary, Cy3 fluorescence was concentrated at the edge of 3D MTSs in the absence of NIR-II irradiation (Fig. 2E, NIR-II(−)), indicating low penetration efficiency. These results confirmed that NIR-II irradiation effectively improved the permeation capability of LipGel-NMs.

CuO_2 NPs were released from LipGel-NMs after FA-mediated endocytosis in the bladder cancer cells and decomposed into Cu^{2+} by the acidic intracellular environment. Released Cu^{2+} catalyzed over-expressed H_2O_2 intra-bladder cancer cells into $^{\bullet}OH$ *via* the Fenton-like reaction, and induced cell apoptosis. To evaluate intracellular $^{\bullet}OH$ generation, DCFH-DA, a fluorescent probe which is oxidized by ROS to generate DCF with green fluorescence,[44] was incubated with LipGel-NMs treated MB49 cells, which showed intense intracellular DCF fluorescence, whereas negligible intracellular DCF fluorescence was observed for MB49 cells that treated with NC-LipGel-NMs that did not contain CuO_2 (Fig. 3A,

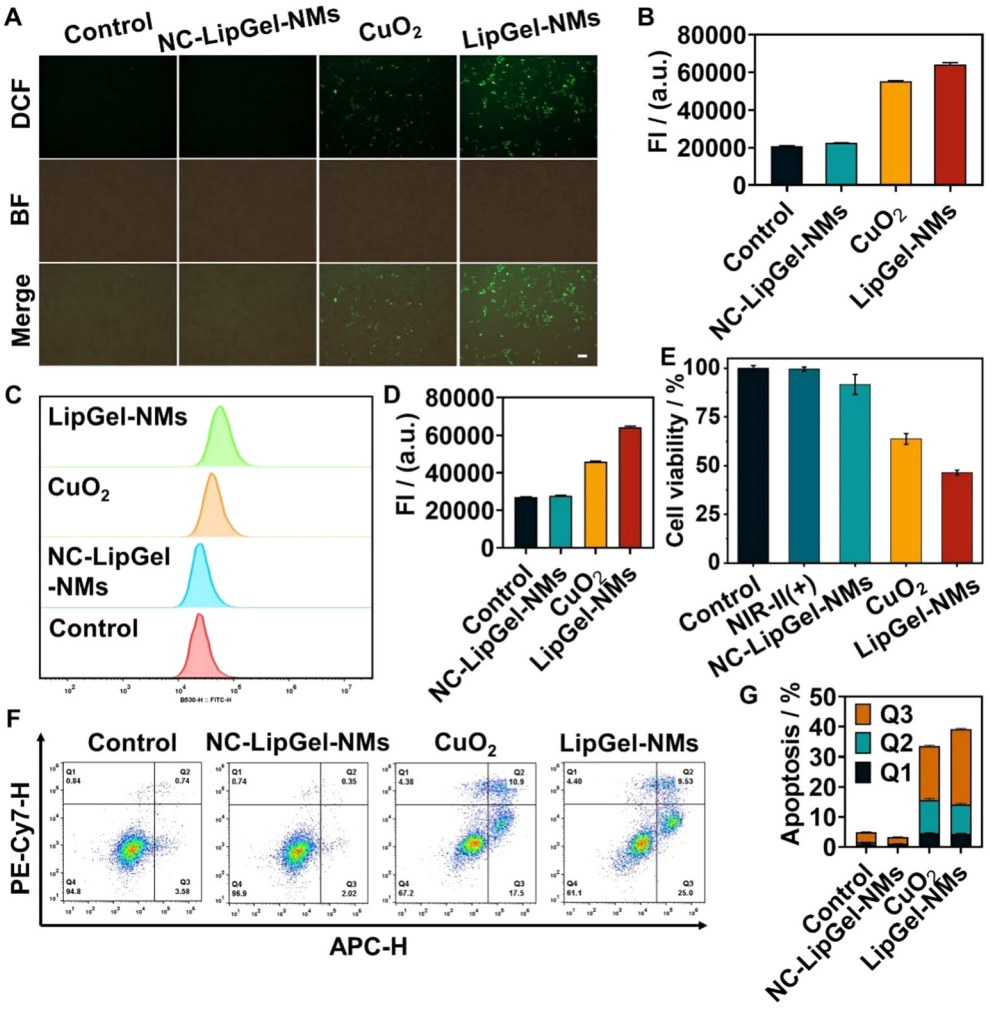

Fig. 3 (A) Fluorescence images and (B) flow cytometry quantification of intracellular DCF fluorescence intensities. Scale bar in (A): 100 μm. (C) Flow cytometry analysis and (D) corresponding quantification of lipid peroxidation (LPO) for MB49 cells incubated with NC-LipGel-NMs, CuO_2 NPs, and LipGel-NMs respectively. (E) Cell viability of MB49 cells treated with merely NIR-II irradiation (NIR-II(+)), NC-LipGel-NMs, CuO_2 NPs, and LipGel-NMs (with equivalent CuO_2 NPs concentration of 10 μg mL^{-1}) in the presence of NIR-II irradiation, respectively. (F) Flow cytometry analysis and (G) corresponding quantification of apoptotic cells for MB49 cells treated with NC-LipGel-NMs, CuO_2 NPs, and LipGel-NMs. Error bars in (E) and (G) indicated means ± SD (n = 3).

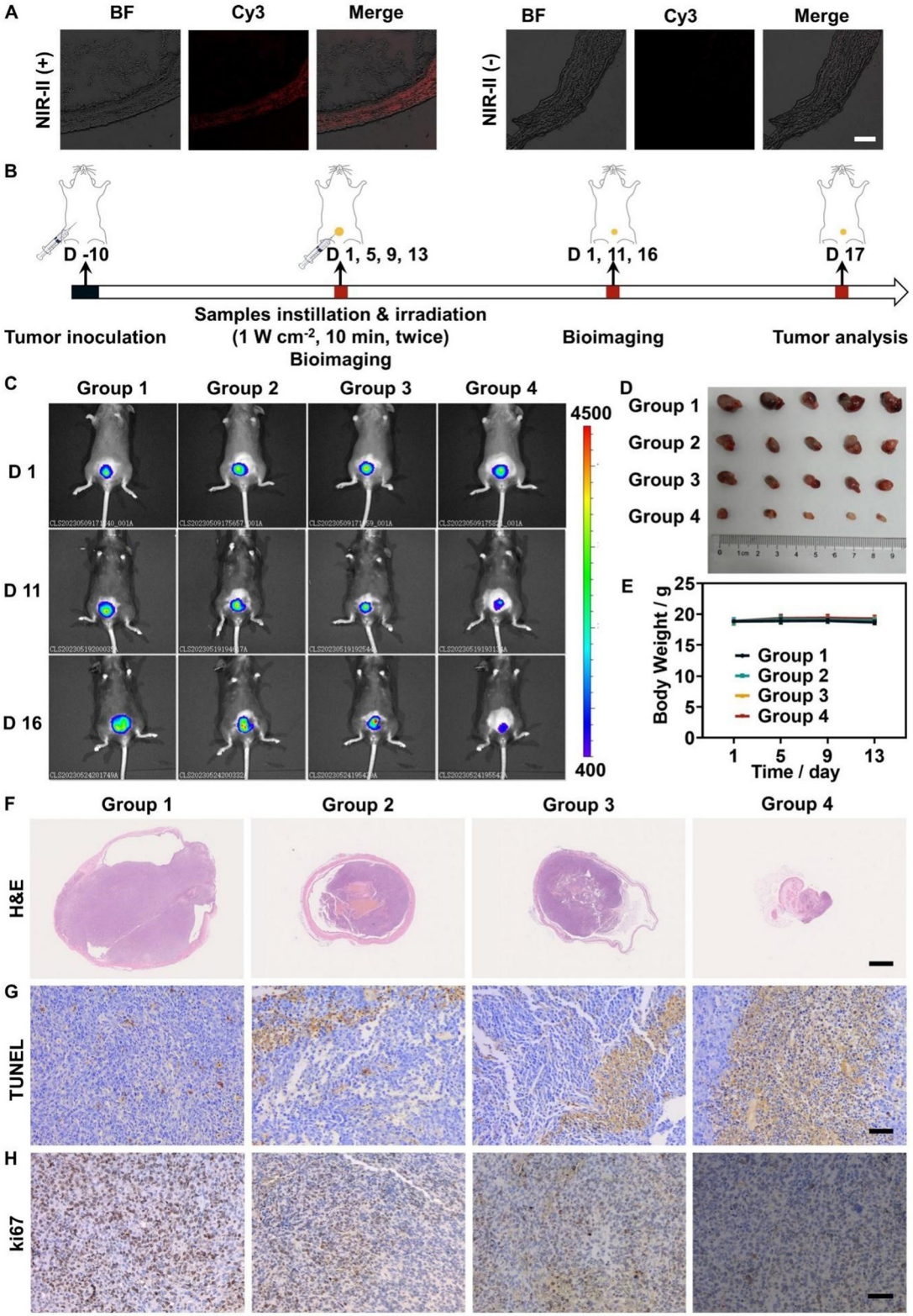

Fig. 4 (A) CLSM images of the bladder section of mice intravesically instilled with LipGel-NMs-Cy3 in the presence (NIR-II(+)) and absence (NIR-II (–)) of NIR-II irradiation (scale bar: 100 μm). (B) Schematic illustration of treatment and therapeutic effect analysis protocols for *in situ* bladder cancer models. (C) Representative fluorescent images on days 1, 11, and 16. (D) Photographs of tumor tissues on day 17, (E) mice weight curves, (F) representative H&E staining images of the whole bladder harvested from sacrificed mice, (G) TUNEL and (H) ki67 staining images of tumor tissues at day 17 for different treatment groups. Group 1–4 in (C–H) represented 1: saline instillation, 2: CuO_2 NPs instillation, 3: LipGel-NMs instillation without NIR-II light irradiation, and 4: LipGel-NMs instillation with NIR-II light irradiation. Scale bars in (F): 1 mm, (G) and (H): 50 μm. Error bars in (E) indicate mean ± SD (n = 5).

LipGel-NMs, NC-LipGel-NMs). MB49 cells that were treated with an equivalent concentration of CuO_2 NPs demonstrated slightly lower intracellular DCF fluorescence compared with MB49 cells that were treated with LipGel-NMs (Fig. 3A, CuO_2 NPs) since the active motion of LipGel-NMs enhanced its endocytosis process. Intracellular $^{\bullet}OH$ generation was also confirmed by flow cytometry, which demonstrated a similar tendency as seen in the micrograph results with the strongest DCF fluorescence for LipGel-NMs treated MB49 cells (Fig. 3B and S17†). Intracellular ROS accumulation results in lipid peroxidation (LPO), which further leads to cancer cell apoptosis.[11,42] C11-BODIPY$^{581/591}$, a fluorescent probe utilized to characterize intracellular lipid peroxidation (LPO) degree was incubated with MB49 cells for localizing ROS accumulation on lipids and demonstrated similar tendency as intracellular DCF fluorescence. Strong intracellular C11-BODIPY fluorescence was observed for both CuO_2 NP-treated MB49 cells and LipGel-NMs-treated MB49 cells, indicating an effective cuproptosis process with CuO_2 NP treatment. A higher C11-BODIPY fluorescence was observed for LipGel-NMs treated MB49 cells compared with CuO_2 NPs treated MB49 cells due to the enhanced endocytosis process of LipGel-NMs from nanomotors' active motion (Fig. 3C and D).

Methyl thiazolyl tetrazolium (MTT) assay was performed to evaluate the therapeutic effect of LipGel-NMs at the cellular level. Merely NIR-II irradiation did not affect cell viability (Fig. 3E, control, NIR-II(+)). In the absence of CuO_2 encapsulation, NC-LipGel-NMs incubation barely demonstrated cytotoxicity in the presence and absence of NIR-II light irradiation, indicating good biocompatibility of LipGel-NMs (Fig. 3E, NC-LipGel-NMs). Both, CuO_2 NPs treatment and LipGel-NMs (CuO_2 concentration fixed at the same as that of CuO_2 NPs of 10 μg mL^{-1}) treatment showed effective cytotoxicity, and LipGel-NMs treated MB49 cells resulted in the lowest cell viability due to the active motion enhanced cellular endocytosis (Fig. 3E, CuO_2, LipGel-NMs). Flow cytometry analysis was also performed to evaluate cell apoptosis, which demonstrated effective cell apoptosis of 33.54% for CuO_2 NPs treated MB49 cells (Fig. 3F and G, CuO_2 NPs) and highest cell apoptosis of 39.23% for LipGel-NMs treated MB49 cells with NIR-II irradiation (Fig. 3F and G, LipGel-NMs). These results guaranteed the efficient therapeutic effect of LipGel-NMs for *in vivo* application.

Intravesical instillation of LipGel-NMs for bladder cancer therapy

The *in situ* bladder cancer model was then constructed to investigate the performance of LipGel-NMs for bladder cancer therapy. Female C57BL/6 mice were randomly divided into two groups, and treated by intravesical instillation of LipGel-NMs-Cy3 under anesthetics in the presence and absence of NIR-II light irradiation. Cy3 fluorescence from bladder sliced sections of the sacrificed mice was monitored to evaluate the permeability of LipGel-NMs. CLSM images demonstrated intense Cy3 fluorescence that occupied nearly all the bladder wall for the NIR-II light irradiation group (Fig. 4A, NIR-II(+)), while negligible Cy3 was observed in the bladder wall in the absence of NIR-II light irradiation (Fig. 4A, NIR-II(−)). These results indicated the active motion of LipGel-NMs contributed to the effective penetration of LipGel-NMs into the mucosal layer of the bladder.

An orthotopic bladder tumor model was established on female C57BL/6 mice to evaluate the *in vivo* antitumor effect of LipGel-NMs. The mice were intravesically instilled with saline, CuO_2 NPs, and LipGel-NMs (2 groups) on days 1, 5, 9, and 13. One of the LipGel-NMs instilled groups was irradiated with 1064 nm NIR-II light after administration. The *in vivo* tumor inhibition effects were determined on the 17th day (Fig. 4B). NIR-II light irradiation resulted in the active motion of LipGel-NMs, which demonstrated a satisfactory anti-tumor effect with obvious inhibition of tumor development (Fig. 4C and D, group 4). Nonpowered LipGel-NMs that in the absence of the NIR-II light irradiation group (Fig. 4C and D, group 3) and CuO_2 NPs treatment group (Fig. 4C and D, group 2) all showed impaired anti-tumor effect due to the lack of NIR-II powering. Mice weights remained stable for all groups during the whole therapeutic period (Fig. 4E). In addition, the H&E staining image also demonstrated much more severe cell damages for the NIR-II light-powered LipGel-NMs group (Fig. 4F and S18,† group 4) compared with nonpowered LipGel-NMs treated group (Fig. 4F and S18,† group 3) and CuO_2 NP-treated group (Fig. 4F and S18,† group 2). The TUNEL experiment also demonstrated the highest level of brown color from the NIR-II light-powered LipGel-NMs group (Fig. 4G, group 4). Ki67 staining images demonstrated the lowest level of brown color from the NIR-II light-powered LipGel-NMs group (Fig. 4H, group 4). These results indicated an effective therapeutic effect for the LipGel-NMs treated mice group with NIR-II laser irradiation. H&E staining histopathology analysis of major organs (heart, liver, spleen, lung, and kidney) harvested from mice on day 17 from all the treatment groups exhibited little lesion compared with the untreated control group (Fig. S19†), indicating the satisfactory *in vivo* biocompatibility of LipGel-NMs. These results confirmed that NIR-II light-powered LipGel-NMs motion effectively facilitated chemodynamic therapy, which would be competent as an instillation reagent and potentially contribute to bladder cancer therapy.

Conclusions

In summary, we developed a 1064 nm NIR-II light-powered hydrogel nanomotor as an intravesical instillation reagent for bladder cancer therapy. The hydrogel nanomotor was prepared by encapsulating chemodynamic therapeutic reagent CuO_2 nanoparticles and core–shell structured Fe_3O_4@Cu_9S_8 nanoparticles in hydrogel nanoparticles and wrapping them with a lipid bilayer (LipGel-NM). CuO_2 nanoparticles worked as CDT reagents to generate ROS for bladder cancer therapy. Fe_3O_4@Cu_9S_8 nanoparticles had asymmetric distribution in nanoparticles, which generated asymmetric heat distribution under NIR-II light irradiation to propel LipGel-NM to penetrate

deeply into the mucosa layer of the bladder wall and effectively enhance the therapeutic effect. The as-reported NIR-II light-powered hydrogel nanomotors exhibited great potential as drug delivery systems in clinical applications. Considering the heat effect of nanomotors can generate immunogenic cell death, the thermophoretic nanomotor can be combined and applied with immunotherapy. These characteristics make self-thermophoretic MNMs very attractive in cancer therapy.

Author contributions

Wei Chen and Yingfei Wang conceived the research idea, and performed experiments. Hao Hu, Yu Zhu and Hongxia Zhao helped with the synthesis and characterization of materials. Yingfei Wang, Wei Chen and Ying Liu wrote the paper. All authors discussed the results, analyzed the data, and reviewed the manuscript.

Conflicts of interest

There are no conflicts to declare.

Acknowledgements

We gratefully acknowledge the National Natural Science Foundation of China (22374073, 82373266, and 82072822), and State Key Laboratory of Analytical Chemistry for Life Science (5431ZZXM2204, 5431ZZXM2307, SKLACLS2413).

References

1 E. Comperat, M. B. Amin, R. Cathomas, A. Choudhury, M. De Santis, A. Kamat, A. Stenzl, H. C. Thoeny and J. A. Witjes, *Lancet*, 2022, **400**, 1712–1721.
2 J. Ferlay, I. Soerjomataram, R. Dikshit, S. Eser, C. Mathers, M. Rebelo, D. M. Parkin, D. Forman and F. Bray, *Int. J. Cancer*, 2015, **136**, E359–E386.
3 H. Sung, J. Ferlay, R. L. Siegel, M. Laversanne, I. Soerjomataram, A. Jemal and F. Bray, *CA-Cancer J. Clin.*, 2021, **71**, 209–249.
4 L. Tran, J. F. Xiao, N. Agarwal, J. E. Duex and D. Theodorescu, *Nat. Rev. Cancer*, 2021, **21**, 104–121.
5 W. S. Tan and J. D. Kelly, *Nat. Rev. Urol.*, 2018, **15**, 667–685.
6 P. Zhang, G. Wu, D. Zhang and W. F. Lai, *J. Controlled Release*, 2023, **354**, 69–79.
7 P. Guo, L. Wang, W. Shang, J. Chen, Z. Chen, F. Xiong, Z. Wang, Z. Tong, K. Wang, L. Yang, J. Tian and W. Xu, *ACS Appl. Mater. Interfaces*, 2020, **12**, 54367–54377.
8 W. H. Chen, K. J. Yu, J. W. Jhou, H. H. Pang, W. H. Weng, W. S. Lin and H. W. Yang, *ACS Appl. Bio Mater.*, 2021, **4**, 7485–7496.
9 W. Lin, H. Liu, L. Chen, J. Chen, D. Zhang, Q. Cheng, F. Yang, Q. Zeng and T. Chen, *Nano Today*, 2021, **38**, 101124.
10 A. Qi, C. Wang, S. Ni, Y. Meng, T. Wang, Z. Yue, K. Yang, Y. Li, Z. Cheng, P. Guo and C. Zhang, *ACS Appl. Mater. Interfaces*, 2021, **13**, 52374–52384.
11 Y. C. Chin, L. X. Yang, F. T. Hsu, C. W. Hsu, T. W. Chang, H. Y. Chen, L. Y. Chen, Z. C. Chia, C. H. Hung, W. C. Su, Y. C. Chiu, C. C. Huang and M. Y. Liao, *J. Nanobiotechnol.*, 2022, **20**, 373.
12 G. Li, S. Wu, W. Chen, X. Duan, X. Sun, S. Li, Z. Mai, W. Wu, G. Zeng, H. Liu and T. Chen, *Small Methods*, 2023, e2201313, DOI: **10.1002/smtd.202201313**.
13 J. Wang, P. Yang, D. Hou, Y. Yan, K. Yue, W. Zhong, T. Xiao, X. Wu, Z. Wang, P. Wu, L. Wang, H. Wang and W. Xu, *Nano Today*, 2022, **45**, 101551.
14 Y. Wang, Y. Zhang, P. C. Li, J. Guo, F. Huo, J. Yang, R. Jia, J. Wang, Q. Huang, D. Theodorescu, H. Yu and C. Yan, *Cancer Res.*, 2022, **82**, 1128–1139.
15 R. C. Walshaw, J. Honeychurch, T. M. Illidge and A. Choudhury, *Nat. Rev. Urol.*, 2018, **15**, 251–259.
16 G. Li, T. Tao, D. Deng, S. Zhang, Y. Chao, Y. Dai, Y. Li, R. Tao, S. Yuan, Z. Liu and S. Wu, *Biomaterials*, 2022, **283**, 121422.
17 K. Ding, L. Wang, J. Zhu, D. He, Y. Huang, W. Zhang, Z. Wang, A. Qin, J. Hou and B. Z. Tang, *ACS Nano*, 2022, **16**, 7535–7546.
18 Y. Hao, Y. Chen, X. He, R. Han, C. Yang, T. Liu, Y. Yang, Q. Liu and Z. Qian, *Biomaterials*, 2022, **293**, 121975.
19 B. Sun, J. N. Bte Rahmat, H. J. Kim, R. Mahendran, K. Esuvaranathan, E. Chiong, J. S. Ho, K. G. Neoh and Y. Zhang, *Adv. Sci.*, 2022, **9**, e2200731.
20 M. Ashrafizadeh, A. Zarrabi, H. Karimi-Maleh, A. Taheriazam, S. Mirzaei, M. Hashemi, K. Hushmandi, P. Makvandi, E. N. Zare, E. Sharifi, A. Goel, L. Wang, J. Ren, Y. N. Ertas, A. P. Kumar, Y. Wang, N. Rabiee, G. Sethi and Z. Ma, *Bioeng. Transl. Med.*, 2022, e10353, DOI: **10.1002/btm2.10353**.
21 Z. Liang, Y. Tu and F. Peng, *Adv. Healthcare Mater.*, 2021, **10**, e2100720.
22 X. Chang, Y. Feng, B. Guo, D. Zhou and L. Li, *Nanoscale*, 2022, **14**, 219–238.
23 W. Xu, H. Qin, H. Tian, L. Liu, J. Gao, F. Peng and Y. Tu, *Appl. Mater. Today*, 2022, **27**, 101482.
24 M. Wan, T. Li, H. Chen, C. Mao and J. Shen, *Angew. Chem., Int. Ed.*, 2021, **60**, 13158–13176.
25 H. Choi, S. H. Cho and S. K. Hahn, *ACS Nano*, 2020, **14**, 6683–6692.
26 J. Wang, Z. Xiong, J. Zheng, X. Zhan and J. Tang, *Acc. Chem. Res.*, 2018, **51**, 1957–1965.
27 K. Villa and M. Pumera, *Chem. Soc. Rev.*, 2019, **48**, 4966–4978.
28 S. Liu, L. Lin and H. B. Sun, *ACS Nano*, 2021, **15**, 5925–5943.
29 B. Chen, M. Ding, H. Tan, S. Wang, L. Liu, F. Wang, H. Tian, J. Gao, Y. Ye, D. Fu, J. Jiang, J. Ou, D. A. Wilson, Y. Tu and F. Peng, *Appl. Mater. Today*, 2022, **27**, 101455.

30 M. Chen, Z. Lin, M. Xuan, X. Lin, M. Yang, L. Dai and Q. He, *Angew. Chem., Int. Ed.*, 2021, **60**, 16674–16679.
31 X. Ji, H. Yang, W. Liu, Y. Ma, J. Wu, X. Zong, P. Yuan, X. Chen, C. Yang, X. Li, H. Lin, W. Xue and J. Dai, *ACS Nano*, 2021, **15**, 14218–14228.
32 T. Li, T. Chen, H. Chen, Q. Wang, Z. Liu, L. Fang, M. Wan, C. Mao and J. Shen, *Small*, 2021, **17**, e2104912.
33 J. Shao, S. Cao, D. S. Williams, L. Abdelmohsen and J. C. M. van Hest, *Angew. Chem., Int. Ed.*, 2020, **59**, 16918–16925.
34 H. Tan, B. Chen, M. Liu, J. Jiang, J. Ou, L. Liu, F. Wang, Y. Ye, J. Gao, J. Sun, F. Peng and Y. Tu, *Chem. Eng. J.*, 2022, **448**, 137689.
35 M. Xuan, J. Shao, C. Gao, W. Wang, L. Dai and Q. He, *Angew. Chem., Int. Ed.*, 2018, **57**, 12463–12467.
36 S. Cao, J. Shao, H. Wu, S. Song, M. T. De Martino, I. A. B. Pijpers, H. Friedrich, L. Abdelmohsen, D. S. Williams and J. C. M. van Hest, *Nat. Commun.*, 2021, **12**, 2077.
37 Y. Cao, T. Wu, K. Zhang, X. Meng, W. Dai, D. Wang, H. Dong and X. Zhang, *ACS Nano*, 2019, **13**, 1499–1510.
38 C. Yang, M. R. Younis, J. Zhang, J. Qu, J. Lin and P. Huang, *Small*, 2020, **16**, e2001518.
39 Y. He, S. Guo, Y. Zhang, Y. Liu and H. Ju, *Biomaterials*, 2021, **275**, 120962.
40 Y. Wang, W. Chen, Z. Wang, Y. Zhu, H. Zhao, K. Wu, J. Wu, W. Zhang, Q. Zhang, H. Guo, H. Ju and Y. Liu, *Angew. Chem., Int. Ed.*, 2023, **62**, e202212866.
41 L. S. Lin, T. Huang, J. Song, X. Y. Ou, Z. Wang, H. Deng, R. Tian, Y. Liu, J. F. Wang, Y. Liu, G. Yu, Z. Zhou, S. Wang, G. Niu, H. H. Yang and X. Chen, *J. Am. Chem. Soc.*, 2019, **141**, 9937–9945.
42 Z. Li, C. Wang, C. Dai, R. Hu, L. Ding, W. Feng, H. Huang, Y. Wang, J. Bai and Y. Chen, *Biomaterials*, 2022, **287**, 121668.
43 M. Zhang, D. Yang, C. Dong, H. Huang, G. Feng, Q. Chen, Y. Zheng, H. Tang, Y. Chen and X. Jing, *ACS Nano*, 2022, **16**, 9938–9952.
44 X. Jin, H. Zhao, Z. Chao, X. Wang, Q. Zhang, H. Ju and Y. Liu, *Chem. – Asian J.*, 2022, **17**, e202200296.
45 K. Liang, H. Sun, Z. Yang, H. Yu, J. Shen, X. Wang and H. Chen, *Adv. Funct. Mater.*, 2021, **31**, 2100355.
46 S. Verma and D. Pravarthana, *Langmuir*, 2011, **27**, 13189–13197.
47 Q. Tian, J. Hu, Y. Zhu, R. Zou, Z. Chen, S. Yang, R. Li, Q. Su, Y. Han and X. Liu, *J. Am. Chem. Soc.*, 2013, **135**, 8571–8577.
48 C. A. Lin, R. A. Sperling, J. K. Li, T. Y. Yang, P. Y. Li, M. Zanella, W. H. Chang and W. J. Parak, *Small*, 2008, **4**, 334–341.
49 X. Wang, M. M. Shindel, S. W. Wang and R. Ragan, *Langmuir*, 2010, **26**, 18239–18245.
50 S. He, S. Chen, D. Li, Y. Wu, X. Zhang, J. Liu, J. Song, L. Liu, J. Qu and Z. Cheng, *Nano Lett.*, 2019, **19**, 2985–2992.
51 R. Lv, P. Yang, B. Hu, J. Xu, W. Shang and J. Tian, *ACS Nano*, 2017, **11**, 1064–1072.
52 R. Lv, X. Jiang, F. Yang, Y. Wang, M. Feng, J. Liu and J. Tian, *Biomater. Sci.*, 2019, **7**, 4558–4567.
53 S. Kaushik and A. M. Cuervo, *Nat. Cell Biol.*, 2015, **17**, 759–770.
54 M. Wan, Q. Wang, R. Wang, R. Wu, T. Li, D. Fang, Y. Huang, Y. Yu, L. Fang, X. Wang, Y. Zhang, Z. Miao, B. Zhao, F. Wang, C. Mao, Q. Jiang, X. Xu and D. Shi, *Sci. Adv.*, 2020, **6**, eaaz9014.
55 M. Wan, Q. Wang, X. Li, B. Xu, D. Fang, T. Li, Y. Yu, L. Fang, Y. Wang, M. Wang, F. Wang, C. Mao, J. Shen and J. Wei, *Angew. Chem., Int. Ed.*, 2020, **59**, 14458–14465.
56 H. Chen, T. Li, Z. Liu, S. Tang, J. Tong, Y. Tao, Z. Zhao, N. Li, C. Mao, J. Shen and M. Wan, *Nat. Commun.*, 2023, **14**, 941.